J. Fluid Mech. (2012), *vol.* 713, *pp.* 61–85. © Cambridge University Press 2012
doi:10.1017/jfm.2012.436

Formation process of the vortex ring generated by an impulsively started circular disc

An-long Yang†, Lai-bing Jia and Xie-zhen Yin

Department of Modern Mechanics, University of Science and Technology of China, Hefei, Anhui 230027, PR China

(Received 13 October 2011; revised 23 July 2012; accepted 30 August 2012; first published online 29 October 2012)

We present an experimental study on the axisymmetric vortex ring generated by a thin circular disc. The velocity and vorticity fields are measured by digital particle image velocimetry (DPIV). The finite-time Lyapunov exponent fields and the Lagrangian coherent structures (LCSs) of the vortex flow are computed in order to analyse the transport of the fluid during its formation and identify the boundary of the vortex ring. The volume, circulation and energy of the vortex ring are calculated. It is found that the formation of the vortex ring basically includes three phases: a rapid growth phase, a stable growth phase and a non-axisymmetric phase. In the rapid growth phase (dimensionless time $0 < T_n < 0.2$) during which Taylor's inviscid estimation is valid, the circulation of the vortex ring grows and the translational velocity of the vortex ring decreases. In the stable growth phase ($0.2 < T_n < 4$), the growth rate of the circulation decreases gradually. In the non-axisymmetric phase ($T_n > 4$), the ring loses axisymmetry due to instability. Compared with the vortex ring generated by the laminar flow from an orifice, the one generated by a circular disc always moves with the disc, and the entrained fluid decreases and the saturated circulation increases. The temporal impulse exerted by the moving disc on the fluid is estimated by DPIV measurements and is calculated using the direct momentum conservation method. The momentum of the control volume enclosing the LCS is found to occupy 64–68 % of the entire impulse exerted by the disc on the fluid.

Key words: biological fluid dynamics, propulsion, vortex dynamics

1. Introduction

Vortex rings are fundamental and fascinating hydrodynamic phenomena. A great amount of research has been reported on them. Shariff & Leonard (1992) and Dabiri (2009) provided helpful and accessible reviews, and Saffman (1992) presented the relevant mathematical foundation. Using the digital particle image velocimetry (DPIV) technique, it is now possible to research the formation process of vortex rings quantitatively. The formation process of a vortex ring includes the generation, development and saturation of the ring. There are basically two methods to generate vortex rings: using a piston to push a column of fluid through an orifice or a nozzle, or making a circular disc move impulsively. The former generation mechanism has been analysed systematically by Gharib, Rambod & Shariff (1998), Dabiri & Gharib (2004)

† Email address for correspondence: yaldjr@mail.ustc.edu.cn

https://doi.org/10.1017/jfm.2012.436 Published online by Cambridge University Press

and Dabiri (2009). On the contrary, to our knowledge, the latter has been little studied up to now.

In the case when a vortex ring is generated using a piston–cylinder apparatus, the vorticity concentrates in the boundary layer of the cylinder wall. When the piston inside the cylinder moves forward, the boundary layer separates at the cylinder exit and rolls up into a vortex ring that propagates away. The vorticity in the boundary layer of the cylinder wall is supplied into the vortex ring through a jet, and hereafter we call this type of ring a 'jet vortex ring'. The process of vortex ring formation is completed when the vortex ring is no longer able to entrain additional vorticity from the jet. This state is referred to as 'vortex ring pinch-off' (Gharib *et al.* 1998).

Gharib *et al.* (1998) proposed that the maximal circulation the vortex ring attains during its formation is reached at a dimensionless time T_n or 'formation number', defined as $T_n = Ut/D$, where U is the piston velocity, T is the duration of the piston stroke and D is the piston diameter. This maximal circulation was found to be in a narrow range $3.6 < T_n < 4.5$ for a number of cases differing in the velocity programme and the diameter of the piston. They suggested that this limiting process is the outcome of the Kelvin–Benjamin variational principle for steady axis-touching vortex rings. They also proposed that there is a lower limit of the dimensionless energy of the jet vortex ring (the dimensionless energy is defined in § 5). If the dimensionless energy of the vorticity flux $\alpha(t) < \alpha_{lim}$, vortex rings will either shed vorticity or accept no extra vorticity in order to maintain $\alpha_{vortex\ ring} = \alpha_{lim}$ within a single ring. Rosenfeld, Rambod & Gharib (1998) confirmed and extended the experimental findings of Gharib *et al.* (1998) using computational fluid dynamics techniques. For thin shear layers, the formation number was confirmed to be approximately equal to 4 for a wide range of cases differing in the discharge time (piston stroke ratio), velocity programme, generator configuration and Reynolds number. Additional cases indicated that a major source of the small variations in the formation number is the different evolution of the velocity profile of the discharged flow. Linden & Turner (2001) got two maximum length-to-diameter L/D (which is equivalent to T_n) ratios ($L/D = 7.83$ matching the properties of the ejected fluid, the energy, impulse and circulation for the Norbury class of rings; and $L/D = 3.5$, adding on the constraint of the volume conservation) of the plug such that a single vortex can be formed. These results showed that the limit implied by matching the energy, impulse and circulation for the Norbury class of rings has not been reached, and it is the volume constraint that is the determining factor. The latter is quite close to the value obtained experimentally by Gharib *et al.* (1998). Dabiri (2009) reviewed the concept of optimal vortex formation and examined its relevance to propulsion in biological and bio-inspired systems. By using examples from the existing literature, he showed that optimal vortex formation can potentially serve as a unifying principle to understand the diversity of solutions used to achieve propulsion in nature. It should be noted that the fluid transport process is very important for the discussion of the vortex formation time. As was mentioned by Linden & Turner (2001), some of the ejected fluid with energy and impulse cannot be transported with the ring. Therefore, it must affect the limiting value of the length-to-diameter ratio.

Dabiri & Gharib (2004) obtained a quantitative result for the entrainment process of the jet vortex ring, using a coaxial counter-flow to retard the translation of vortex rings generated from a piston–cylinder apparatus. In the absence of counter-flow, the magnitude of fluid entrainment was determined directly by determining the boundary of the ring and found to lie between 30 and 40 % of the volume of the vortex ring. However, the determination of the edge of the ring in this manner is difficult.

https://doi.org/10.1017/jfm.2012.436 Published online by Cambridge University Press

Haller (2001, 2002), Shadden, Lekien & Marsden (2005), Shadden, Dabiri & Marsden (2006) and Shadden *et al.* (2007) among others have demonstrated that, by computing the finite-time Lyapunov exponent (FTLE) field corresponding to the flow of interest, one can identify Lagrangian coherent structures (LCSs). LCSs represent almost-invariant boundaries that separate fluid with different dynamic behaviours. LCSs have been used to define the boundary and structure of vortices in laminar and turbulent flow in Shadden *et al.* (2006) and Green, Rowley & Haller (2007). In the case of vortex rings, the ridges of local maximal in the FTLE field demarcate the vortex boundary.

There has been only limited study of the starting vortex ring produced by a translating disc. Taylor (1953) deduced the parameters of the vortex ring theoretically by giving an impulse to a circular disc and then 'dissolving' it away in a perfect fluid without separation of flow. According to Taylor's derivation, the dimensionless circulation Γ_n of the disc vortex ring is $4/\pi \approx 1.27$, the ratio of the vortex translational speed to the disc speed is 0.436, and the ratio of the vortex ring radius to the disc radius is 0.816. Sallet (1975) studied experimentally a vortex ring caused by impulsive motion of a circular disc. The parameters of the developed vortex ring, such as circulation, volume, impulse, energy and vortex translational speed, were measured. Sallet found that the dimensionless circulation Γ_n of the disc vortex ring is $\sim$4, the ratio of the vortex translational speed to the disc speed is $\sim$1.1, and the ratio of the vortex ring radius to the disc radius is $\sim$1.2 in experiments. Although Sallet (1975) did not show the measuring time of the results, we guessed that Sallet's results could be measured when the vortex ring has been fully developed. There were discrepancies between Taylor's derivation and Sallet's experimental results, since Taylor's derivation could only be used to estimate the physical quantity at the beginning of the disc vortex formation process.

Shenoy & Kleinstreuer (2008) performed the computation of viscous flow over a circular disc of aspect ratio (thickness/diameter) equal to 10 in the Reynolds number (Re) range of 10–300. Their simulations suggested that the flow over a circular disc is periodic three-dimensional for $155 < Re \leqslant 300$. Their simulations also suggested that the flow of the starting vortex ring produced by a translating disc could change from an axisymmetric state to a periodic three-dimensional state. The parameters of the vortex ring generated by an impulsively started circular disc have not been measured in detail and the whole vortex ring formation process has not yet been studied.

Dabiri (2009) argued that the concept of optimal vortex formation could be regarded as a principle in biological propulsion. Using a piston to push a column of fluid through an orifice or a nozzle is similar to the ring generation mechanisms of many swimming animals such as salps, jellyfish and medusa. The ring generated by the impulsive motion of a circular disc is similar to that produced by a swimming fish or a flying bird. The goal of this paper is to determine whether these different mechanisms lead to a similar formation process and whether the optimal vortex formation is universal. Both processes lead to a starting axisymmetric vortex ring with a circulation that reaches saturation. However, there are five discrepancies between the jet vortex ring and the disc vortex ring: (i) The jet vortex ring has an obvious saturation characteristic, named 'pinch-off', but the disc vortex ring does not. (ii) The vorticity flux is entrained into the jet vortex ring along the symmetry axis, while it is entrained into the disc vortex ring from the outer edges of the ring. (iii) For the jet vortex ring, the vorticity flux from the nozzle is almost constant; while for the disc vortex ring, the vorticity flux from the edge of the circular disc varies with time. (iv) The jet vortex ring moves away from the vortex generator and can be treated as an isolated vortex ring; but the disc vortex ring moves with the disc and, as a result, the disc becomes

https://doi.org/10.1017/jfm.2012.436 Published online by Cambridge University Press

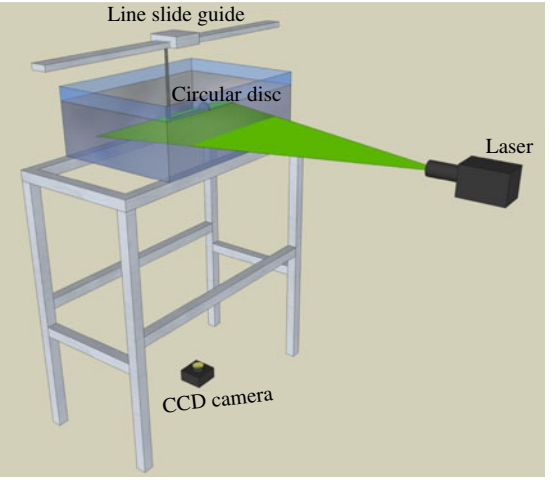


FIGURE 1. (Colour online) Schematic of the apparatus.

a boundary of the vortex ring. (v) The jet the nozzle cannot be entrained into the jet vortex ring immediately. The time during which the jet vortex ring entrains the vorticity flux is about twice that of the nozzle ejecting the same vorticity flux (Gharib *et al.* 1998; Shadden *et al.* 2007). In contrast, the process of ejecting the flux from the edge of the disc is synchronous with the process of entraining the flux into the vortex ring.

The purpose of the present study is to analyse the formation and growth of the starting disc vortex ring and to compare it with the jet flow starting vortex ring. The paper is organized as follows. In § 2, the experimental apparatus, the DPIV method and the calculation of the FTLE field and LCSs are presented. In § 3, LCSs are used to analyse the fluid entrainment and flux window (the flux window is defined in § 3) during the formation of the ring based on DPIV data. In §§ 4 and 5, the boundary, volume, circulation and energy of the disc vortex ring are calculated and the position of the vortex core is measured. In § 6, the flow field of the vortex ring for the dimensionless time $T_n > 5$ is investigated. In § 7 the approaches to estimate the variation of the impulse exerted by the disc on the fluid with time based on data of DPIV measurements are presented. Finally, the main conclusions are drawn.

2. Experimental methods and procedures

2.1. *Apparatus*

The apparatus generating the starting vortex ring in the experiment is shown in figure 1. A circular disc with diameter $D = 30$ mm and thickness $\delta = 2$ mm is immersed in a 25 cm $\times$ 25 cm $\times$ 70 cm ($H \times W \times L$) water tank. The motion of the disc is driven by a slipper block mounted on a screw rod controlled by a DC motor. The accuracy of the DC motor speed is restricted by the motor driver, and the experiment possesses good repeatability ($\Delta L/L < 0.09\,\%$, $L \approx 4D$, L represents the stroke length of the disc, ΔL represents the discrepancy of the stroke length between two runs during the same period of time).

The flow field of the disc vortex ring is recorded quantitatively using time-resolved digital particle image velocimetry (TR-DPIV) (Willert & Gharib 1991)

https://doi.org/10.1017/jfm.2012.436 Published online by Cambridge University Press

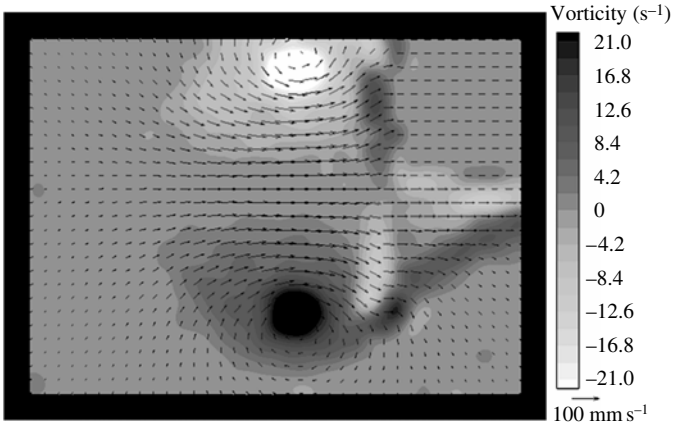


FIGURE 2. Velocity vector and vorticity of the vortex ring in a symmetrical plane.

on apparatus assembled in our laboratory. The water tank is seeded with 1–5 μm diameter glass spheres, and a small quantity of salt is dissolved in the water to adjust the density of the water (the particles remain suspended for 30 min). A 5 W continuous semiconductor laser with wavelength of 532 nm is used to produce a light sheet through a cylindrical lens, which illuminates the horizontal symmetric plane of the disc. The light scattered from the suspended particles is captured by a 640 pixel × 480 pixel monochromatic charge-coupled device (CCD) digital camera at 200 frame s^{-1} (for $U = 13.9$ and 9.39 cm s^{-1}) and at 140 frame s^{-1} (for $U = 6.77$ and 5.28 cm s^{-1}), respectively. The pixel resolutions correspond approximately to a physical test section resolution of 0.105 mm × 0.105 mm (for $U = 13.9$, 9.39 and 6.77 cm s^{-1}) and 0.0787 mm × 0.0787 mm (for $U = 5.28$ cm s^{-1}), respectively, sufficient to resolve the vorticity distribution of the vortex ring core. In the experiments, each pair of images represents a time interval of 5 ms (for 200 frame s^{-1}) or 7.143 ms (for 140 frame s^{-1}), and the area measured by the CCD is approximately 6.7 cm × 5.0 cm (for resolution of 0.105 mm × 0.105 mm) or 5.0 cm × 3.8 cm (for resolution of 0.0787 mm × 0.0787 mm).

The interrogation is accomplished using a window size of 33 pixel × 33 pixel with a 50 % overlap. The calculation of the velocity and vorticity fields is completed using an in-house code on an Intel 2.66 GHz processor. The measurements of velocity and vorticity possess an uncertainty of 1 and 3 %, respectively. The Reynolds number of the flow ranges from 1600 to 4200 based on the disc speed and diameter.

2.2. *Image matching and velocity data interpolation*

The instantaneous velocity and vorticity fields generated by a thin circular disc are illustrated in figure 2, where the arrows indicate the velocity and the greyscale map is for the vorticity. The thin disc moves to the right, the cores of the generated vortex ring being visualized as two circles with opposite vorticity in the symmetrical plane. Since the starting vortex ring generated by the thin disc is highly axisymmetric, as is shown in figure 2, we only need to analyse the instantaneous velocity and vorticity fields of the half vortex ring in the symmetry plane.

Owing to the limitation of the field of vision and the image resolution of the CCD digital camera, the whole formation process of the vortex ring caused by the impulsive motion of a circular disc cannot be recorded in a single position. Considering the good

https://doi.org/10.1017/jfm.2012.436 Published online by Cambridge University Press

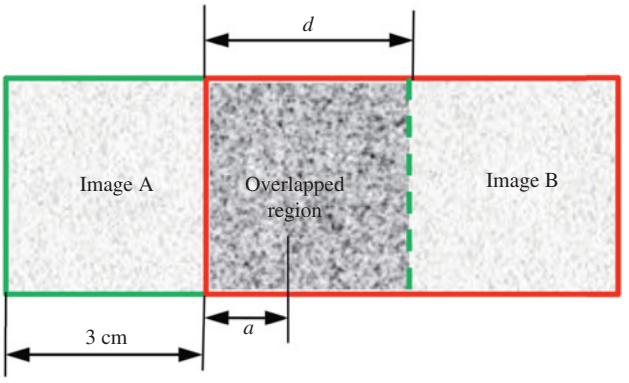


FIGURE 3. (Colour online) Schematic of the linear interpolation in the overlapped region of the velocity field.

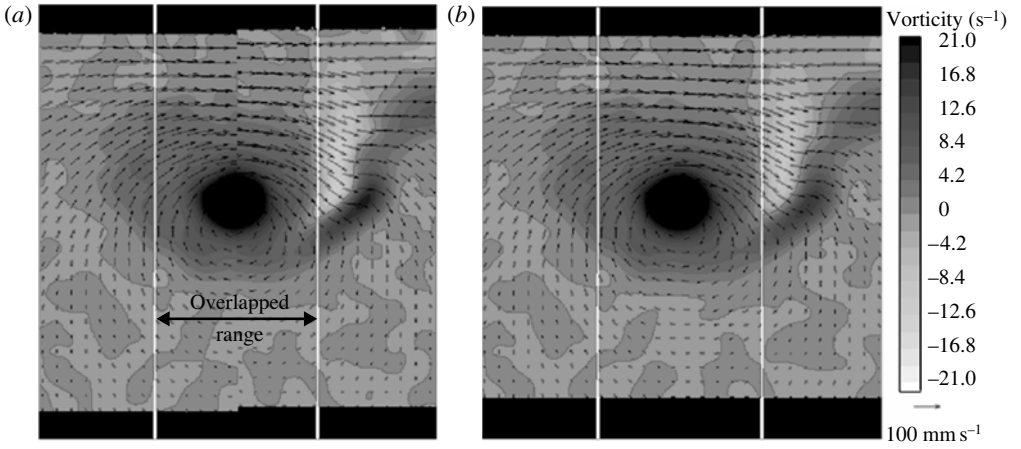


FIGURE 4. Velocity vector and vorticity of two adjacent velocity fields for $U = 5.28$ cm s^{-1}. (a) The result before interpolation; (b) the result after interpolation.

repeatability of the disc vortex ring experiments, we record the images and measure the flow fields at several positions, and then reconstruct the panorama of the vortex ring formation. The average relative error of the velocity $|U_A - U_B|/U$, with U the disc speed, is less than 3 % in the overlapped region, as is shown in figure 3, which is slightly larger than the uncertainty (1 %) of the DPIV velocity measurements. In a set of experiments, the CCD camera is set accurately at eight positions, 3 cm apart, and located in advance, parallel to the direction of motion of the circular disc.

Figure 3 shows the scheme of the linear interpolation of the velocity field in the overlapped region of two adjacent images A and B obtained by DPIV. Both images are of size 5.0 cm × 3.8 cm with an offset of 3 cm. Figure 4(a) shows the velocity and vorticity fields of the two adjacent images A and B. It can be seen that a slight discrepancy exists in the overlapped region there. In particular, the vorticity in the overlapped region is discontinuous. In order to maintain the continuity of the velocity

https://doi.org/10.1017/jfm.2012.436 Published online by Cambridge University Press

and vorticity fields, a linear interpolation

$$U_{OL} = \frac{d-a}{d} U_A + \frac{a}{d} U_B \tag{2.1}$$

is applied, where U_{OL} is the interpolated velocity in the overlapped region of two images, d is the width of the overlapped region, a is the distance of the measured point from the left boundary, and U_A and U_B are the velocities of the regions A and B, respectively. The resultant velocity and vorticity fields after interpolation are shown in figure 4(*b*). More details can be found in Yang, Jia & Yin (2010).

2.3. *Finite-time Lyapunov exponent field and vortex boundary identification*

To determine the vortex ring boundary, we employ a Lagrangian criterion based on the distribution of the FTLE field (Shadden *et al.* 2005, 2006, 2007) (also referred to as the direct Lyapunov exponent field, see Haller (2001)). Since the flow of the disc vortex ring is unsteady and has obvious Lagrangian coherent structures (LCSs), the boundary of the vortex is determined by tracking the relative Lagrangian trajectories of the individual fluid particles in the flow. This FTLE approach is simpler than and compatible with the other methods used to locate LCSs in time-dependent flows.

The FTLE measures the maximum stretching about a material point over a chosen time interval. More precisely, let $\phi_t^{t+T} : \boldsymbol{x}(t) \to \boldsymbol{x}(t+T)$ denote the mapping of a material point located at $\boldsymbol{x}(t)$ at time t to its position at time $t+T$. The FTLE is defined as

$$\sigma(x, t, T) \triangleq \frac{1}{|T|} \ln \sqrt{\lambda_{max}(\Delta(\boldsymbol{x}, t, T))}, \tag{2.2}$$

where λ_{max} denotes the maximum eigenvalue of $\Delta(\boldsymbol{x}, t, T)$, the finite-time Cauchy–Green deformation tensor:

$$\Delta(\boldsymbol{x}, t, T) = \frac{\mathrm{d}\phi_t^{t+T}(x)}{\mathrm{d}x}^T \frac{\mathrm{d}\phi_t^{t+T}(x)}{\mathrm{d}x}. \tag{2.3}$$

In (2.2) $|T|$ is used because that the computation for $T > 0$ and $T < 0$ produces forward-time FTLE and backward-time FTLE akin to stable and unstable manifolds, respectively. The FTLE field is used to reveal the LCSs. Within this framework, LCSs are defined as codimension-one structures along which the FTLE field is maximized (Shadden *et al.* 2005). The ridge lines of the forward-time FTLE and backward-time FTLE correspond to the repelling LCS and attracting LCS, respectively.

3. Fluid entrainment and flux window during formation of disc vortex ring

The interpolated velocity data are used to compute the FTLE field via the method described in § 2.3. All the FTLE analyses are performed with particles uniformly spaced 1 pixel (0.0781 mm for $U = 5.28$ cm s^{-1}) apart. Figure 5 shows the forward-time (red ridge lines) and backward-time (blue ridge lines) FTLE fields at a sequence of times, $t = 0.714$, 1.429 and 2.714 s, respectively. The time $t = 0$ corresponds to the instant at which the disc motion started.

As is shown in table 1, the forward integration time ($T > 0$) for three different stages is identically 1.964 s, which is sufficient to get the clear ridge lines of the forward-time FTLE(r-LCS). However, the backward integration time ($T < 0$) for three different stages requires integration times less than or equal to the disc movement time t, which makes it impossible to obtain clear ridge lines of the backward-time

https://doi.org/10.1017/jfm.2012.436 Published online by Cambridge University Press

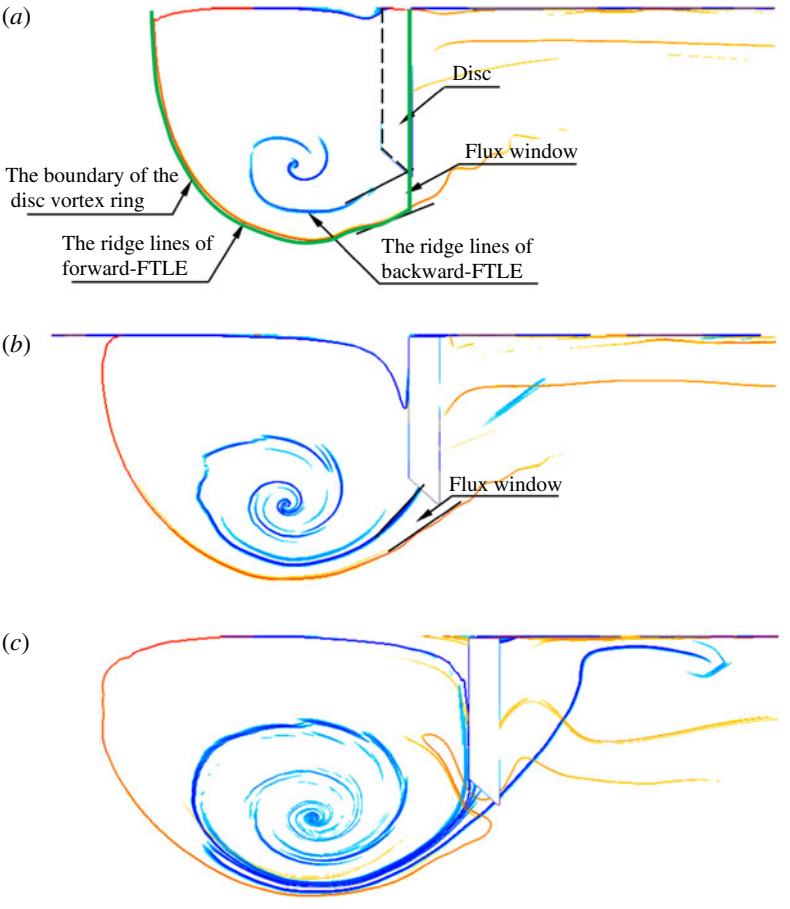


FIGURE 5. The forward-time (red ridge line) and backward-time (blue ridge line) FTLE fields for $U = 5.28$ cm s^{-1} at: (*a*) $t = 0.714$ s, $T_n = Ut/D = 1.26$; (*b*) $t = 1.429$ s, $T_n = Ut/D = 2.52$; and (*c*) $t = 2.714$ s, $T_n = Ut/D = 4.79$.

Figure number	Time t (s)	Forward integration time (s)	Backward integration time (s)	$T_n = Ut/D$
Figure 5(*a*)	0.714	1.964	−0.714	1.26
Figure 5(*b*)	1.429	1.964	−1.429	2.52
Figure 5(*c*)	2.714	1.964	−1.964	4.79

TABLE 1. Arguments of the FTLE at different times. Here t represents the disc movement time, T_n represents the dimensionless time, U represents the disc velocity and D represents the disc diameter.

FTLE(a-LCS) at the beginning of the disc motion. In figure 5 the red ridge line of the r-LCS represents an interface from which particles depart after time T, so it is the left boundary of the vortex ring. The blue ridge line of the a-LCS in the vortex ring

https://doi.org/10.1017/jfm.2012.436 Published online by Cambridge University Press

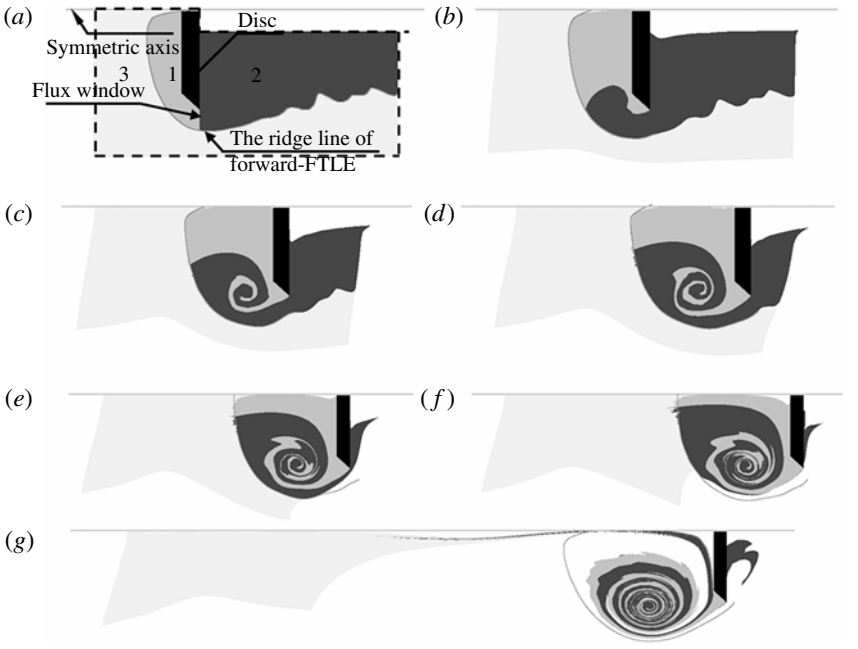


FIGURE 6. Temporal evolution of the fluid parcels for $U = 5.28$ cm s^{-1}: (*a*) $t = 0$ s, $T_n = Ut/D = 0$; (*b*) $t = 0.157$ s, $T_n = 0.277$; (*c*) $t = 0.371$ s, $T_n = 0.654$; (*d*) $t = 0.514$ s, $T_n = 0.905$; (*e*) $t = 0.729$ s, $T_n = 1.28$; (*f*) $t = 0.943$ s, $T_n = 1.66$; (*g*) $t = 2.157$ s, $T_n = 3.80$. In panel (*a*) the box (dashed line) marks the boundary of a parcel of tracers released in the flow. The parcel of tracers is divided into three parts (1, mid-grey/green; 2, dark grey/red; 3, light grey/yellow) by the disc and the ridge line of the r-LCS.

represents a line at which the particles before time T converge, and therefore it is a helical line in the vortex core.

In figure 5, it is clear that fluid separates from the edge of the disc and a vortex rolls up once the disc starts. As the disc moves, the vortex core becomes gradually larger and the vortex ring becomes stronger. It is worth noting that there is a channel between the blue ridge and the red ridge lines in figure 5(*a*,*b*), through which the fluid with vorticity flows into the vortex core continuously. This channel provides a vorticity flux for the starting vortex ring, which is referred to as the 'flux window' hereafter. The flux window may change during the formation of the vortex ring. The larger the dimensionless time T_n, the smaller is the flux window, as shown in figure 5. Particularly, it is nearly closed at the dimensionless time $T_n = 4.71$, as is shown in figure 5(*c*).

In order to further study the fluid entrainment in the formation of the vortex ring, we place fluid particles in a region encircled by the dashed line at moment $t = 0$ (figure 6*a*). In figure 6(*a*) the fluid field is divided into three parts by the ridge line of the forward-time FTLE and the disc: the fluid at the left side of the disc (the mid-grey/green region with label 1), the fluid at the right side of the disc (the dark grey/red region with label 2) and the fluid outside the ridge line (the light grey/yellow region with label 3). Figure 6(*b–g*) shows the flow evolution as the disc moves to the right. The fluid in the dark grey/red region 2 is entrained in the disc vortex ring through the flux window and mixed with the fluid in the mid-grey/green region 1. The

https://doi.org/10.1017/jfm.2012.436 Published online by Cambridge University Press

fluid in the mid-grey/green region, moving together with the disc, is entrained into the vortex core gradually and is contained in the vortex ring throughout. The fluid in the light grey/yellow region 3 is excluded from the disc vortex ring at all times. It is also demonstrated that the ridge line of the forward-time FTLE is a material line through which fluid cannot pass. Owing to the existence of the disc, the flux window between the disc and the ridge line of the forward-time FTLE becomes a unique channel that provides the vorticity flux into the vortex ring. Once the flux window is closed, no new vorticity goes into the vortex ring and the formation of the starting vortex ring terminates. It should be pointed out that the existence of the white region in the vortex ring in figure 6(*g*) occurs because the marked region in figure 6(*a*) is not large enough. If the right boundary of the region is extended, the vacant part will be filled with the fluid in the red region.

4. Determination of the instantaneous boundary and volume of the disc vortex ring

In the jet vortex ring case, the vortex ring sheds from the nozzle and becomes isolated, the r-LCS and the a-LCS being its closed boundary. In the disc vortex ring case, the ring moves with the disc all the time and the disc serves as a boundary of the ring. As is shown in figure 5, the r-LCS and the a-LCS of the vortex ring cannot form a closed surface until the formation process of the disc vortex ring terminates. However, in such a case the disc may be treated as a material surface. Thus a closed surface composed of the r-LCS in the leeward side of the disc, the disc and the flux window is obtained, as is shown in figure 5(*b*) (the green lines). The closed surface is used to identify the instantaneous boundary of the disc vortex ring. The determination of the instantaneous boundary is crucial for the analysis of the formation process of the disc vortex ring, because the temporal macroscopic quantities, such as the volume and the circulation, are calculated utilizing the instantaneous boundary.

Once the boundary of the vortex ring is determined, the volume of the vortex ring is calculated. Figure 7(*a*) shows how the variation of the volume of the vortex ring varies with time for different disc speeds. It is clear in the figure that the volume of the vortex ring increases more rapidly at higher disc speeds. As in the jet vortex ring case, we take $T_c = D/U$ as the characteristic time and define the dimensionless time $T_n = tU/D$. We take the volume of the sphere $V_c = \pi D^3/6$ as the characteristic volume, and define the dimensionless volume $V_n = V/(\pi D^3/6)$. The normalized vortex ring volume is shown in figure 7(*b*), where the curves at different disc speeds are close to each other as a result.

In figure 7(*b*), the dimensionless volume V_n approaches its maximum between 3.1 and 3.4 when the dimensionless time T_n is larger than 4. At this dimensionless time, the flux window is also closed, as is shown in figure 5. Note that the volume of the vortex ring at the initial time $T_n = 0$ ($t = 0$) is the volume of the fluid particles in the mid-grey/green region (labelled 1) in figure 6(*a*). It is the part of the fluid encircled in the vortex ring all the time. The fluid in the dark grey/red region (labelled 2) in figure 6 supplies the vortex ring with vorticity. The total volume of the vortex ring is the sum of the two parts of fluids. According to Dabiri & Gharib (2004), the entrained fluid fraction $\eta(t)$ is equal to the ratio of the fluid volume labelled 1 to the total volume of the vortex ring. The calculation shows that the entrained fluid fraction $\eta(t)$ for the disc vortex ring ranges from 11.7 to 12.4 %. This value is much less than 30–40 % in the jet vortex ring case without counter-flow (Dabiri & Gharib 2004). The reason for this difference could be that in the jet vortex ring case the entrained

https://doi.org/10.1017/jfm.2012.436 Published online by Cambridge University Press

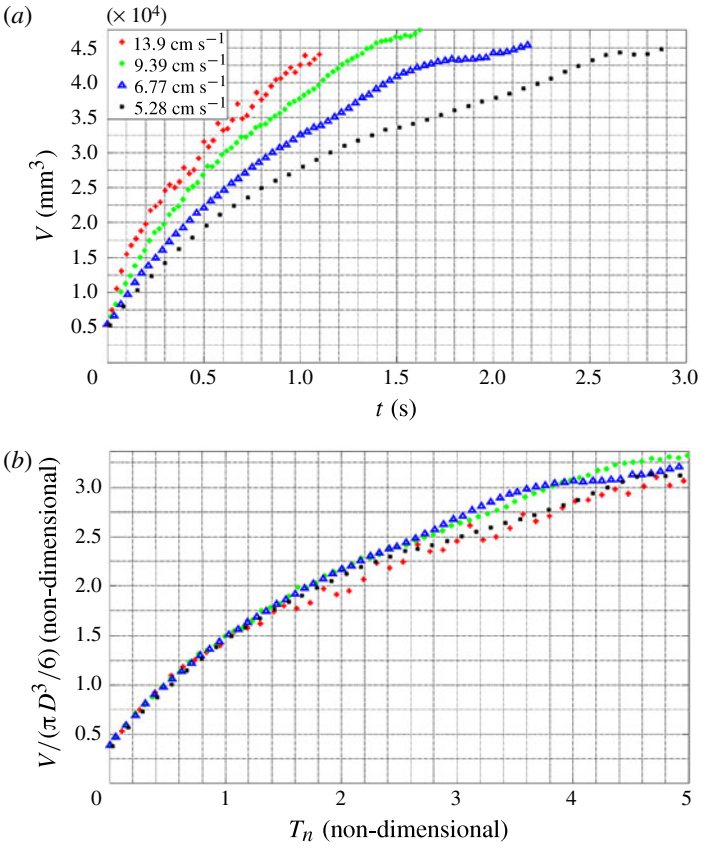


FIGURE 7. (Colour online) Variation of the volume of the disc vortex with time for different disc speeds: (*a*) the dimensional result; (*b*) the dimensionless result. The value at $t = 0$ is the fluid volume inside the r-LCS and in the downwind side of the disc (the mid-grey/green area in figure 6*a*).

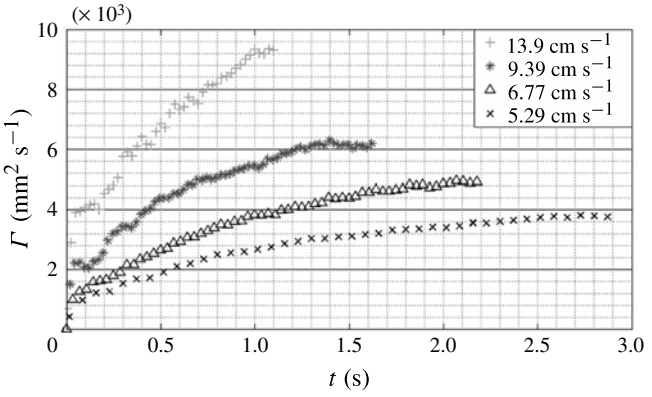
fluid enters into the vortex ring through convection and diffusion across the entire ring surface, while in the disc vortex ring case the entrained fluid is restricted in the region of the ring downstream of the disc and its volume is decreased greatly.

5. Circulation, energy and position of the vortex core

The circulation that represents the strength of a vortex ring can be calculated based on the DPIV results. Figure 8 shows the time evolution of the circulation for different disc speeds. Similar to the volume of the ring shown in figure 7(*a*), the circulation arrives at its maximum more rapidly for larger speeds. To analyse the mechanism during the disc vortex formation process, we normalize the circulation using the specific circulation $\Gamma_c = UD/2$ as in the jet vortex ring case. Figure 8(*b*) shows the dimensionless circulation $\Gamma_n = \Gamma/\Gamma_c$. Clearly the evolution of Γ_n at different disc speeds has the same trend, implying that the formation process of the disc vortex ring at different Reynolds numbers has the same trend in experiments. We fit the experimental data with $\Gamma_n = a[1 - de^{-bT} - (1 - de^{-cT})]$, where a represents the maximum dimensionless circulation ranging from 4.6 to 5.1 in our experiments, and

https://doi.org/10.1017/jfm.2012.436 Published online by Cambridge University Press

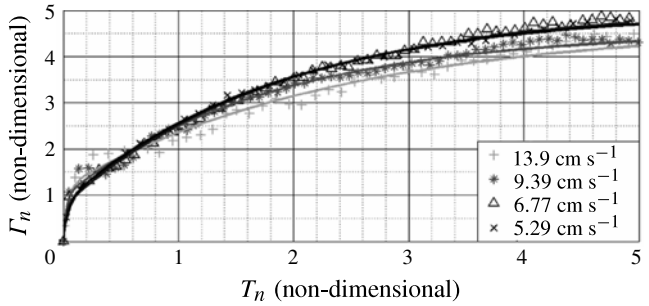
(*a*)



+	$y = a(1 - d\,\mathrm{e}^{-bx} - (1-d)\,\mathrm{e}^{-cx})$	$a = 4.67$	$b = 0.416$	$c = 24.927$	$d = 0.750$	Resnorm = 1.38
∗	$y = a(1 - d\,\mathrm{e}^{-bx} - (1-d)\,\mathrm{e}^{-cx})$	$a = 4.56$	$b = 0.553$	$c = 39.666$	$d = 0.786$	Resnorm = 1.10
Δ	$y = a(1 - d\,\mathrm{e}^{-bx} - (1-d)\,\mathrm{e}^{-cx})$	$a = 5.06$	$b = 0.522$	$c = 39.297$	$d = 0.848$	Resnorm = 0.61
×	$y = a(1 - d\,\mathrm{e}^{-bx} - (1-d)\,\mathrm{e}^{-cx})$	$a = 4.98$	$b = 0.535$	$c = 22.452$	$d = 0.830$	Resnorm = 0.19

Resnorm-all = 3.29

(*b*)



+	$y = a(db\,\mathrm{e}^{-bx} + (1-d)\,c\,\mathrm{e}^{-cx})$	$a = 4.67$	$b = 0.416$	$c = 24.927$	$d = 0.750$	Resnorm = 1.38
∗	$y = a(db\,\mathrm{e}^{-bx} + (1-d)\,c\,\mathrm{e}^{-cx})$	$a = 4.56$	$b = 0.553$	$c = 39.666$	$d = 0.786$	Resnorm = 1.10
Δ	$y = a(db\,\mathrm{e}^{-bx} + (1-d)\,c\,\mathrm{e}^{-cx})$	$a = 5.06$	$b = 0.522$	$c = 39.297$	$d = 0.848$	Resnorm = 0.61
×	$y = a(db\,\mathrm{e}^{-bx} + (1-d)\,c\,\mathrm{e}^{-cx})$	$a = 4.98$	$b = 0.535$	$c = 22.452$	$d = 0.830$	Resnorm = 0.19

Resnorm-all = 3.29

(*c*)

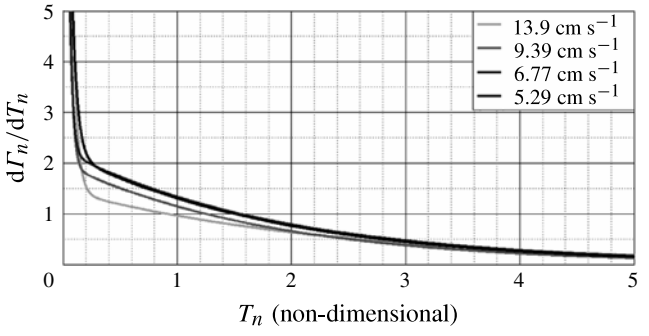


FIGURE 8. Variation of the circulation of the disc vortex ring for different disc speeds: (*a*) the dimensional result; (*b*) the dimensionless result. The points represent the experimental data and the solid lines are the fitting results. (*c*) The dimensionless growth rate of the circulation.

https://doi.org/10.1017/jfm.2012.436 Published online by Cambridge University Press

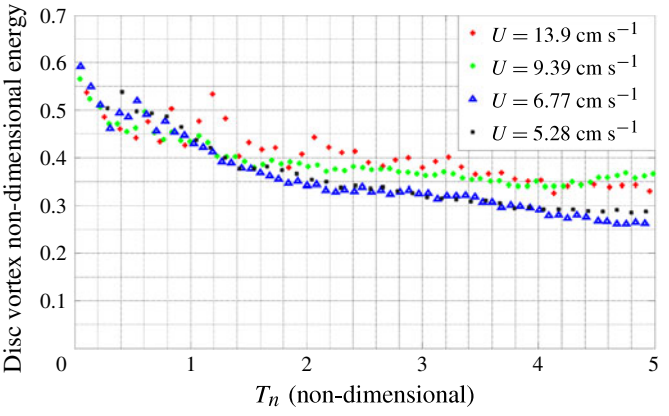


FIGURE 9. (Colour online) Dimensionless energy of the disc vortex ring for the disc speeds $U = 13.9,\ 9.39,\ 6.77,\ 5.28$ cm s^{-1}.

$1/b$ and $1/c$ represent two characteristic times for the growth of the circulation, corresponding to the stable growth phase and rapid growth phase, respectively. The quantities d and $(1 - d)$ represent the ratios of the two circulation components to the total circulation of the disc vortex ring, respectively. The best-fitting curves are plotted in figure 8(*b*) (solid lines). The dimensionless circulation for the disc vortex ring is larger than 1 (3.6–4.5) for the jet vortex ring (Gharib *et al.* 1998). In addition, the derivative of the best-fitting curve $\mathrm{d}\Gamma_n/\mathrm{d}T_n$ is drawn in figure 8(*c*). When the dimensionless time $T_n < 0.2$, the growth rate of the dimensionless circulation is much larger than 1. When the dimensionless time $T_n > 0.2$, the growth rate decreases gradually. In the jet vortex ring case the vortex formation time is equivalent to and numerically equal to the time relative to the 'vortex saturation circulation' that can be estimated on the basis of the slug model. However, the circulation growth rate of the disc vortex ring is inconsistent with the estimation of the slug model. In the present paper, the value of the maximum dimensionless circulation is referred to as the 'vortex saturation circulation' of the disc vortex ring and the corresponding dimensionless time as the formation time of the disc vortex ring.

The growth process of the dimensionless circulation can be roughly divided into two phases for the dimensionless time $T_n < 4$. The first is the rapid growth phase for the dimensionless time $T_n < 0.2$, in which phase the growth rate of the circulation is much larger than that of the jet vortex ring (the growth rate of the circulation of the jet vortex ring equals 1 from beginning to end) and the circulation Γ_n of the disc vortex ring rapidly reaches 1.3–1.7. The second is the stable growth phase at the dimensionless time $0.2 < T_n < 4$. The growth rate in this phase is ∼1–2 at the beginning and decreases gradually. The situation for the dimensionless time $T_n > 4$ will be discussed in § 6.

The dimensionless energy is another important parameter. The dimensionless energy is defined as $\alpha = E/(I^{1/2}\Gamma^{3/2})$ (Gharib *et al.* 1998), where E, I and Γ are the kinetic energy, impulse and circulation, respectively. Setting the density to unity, we have

$$E = \pi \int \omega\psi \,\mathrm{d}x\,\mathrm{d}r, \quad I = \pi \int \omega r^2 \,\mathrm{d}x\,\mathrm{d}r, \quad \Gamma = \int \omega \,\mathrm{d}x\,\mathrm{d}r, \tag{5.1}$$

where ω is the vorticity and ψ is the stream function. The dimensionless energy α can be calculated from the DPIV measurements, and is shown in figure 9. We see that

https://doi.org/10.1017/jfm.2012.436 Published online by Cambridge University Press

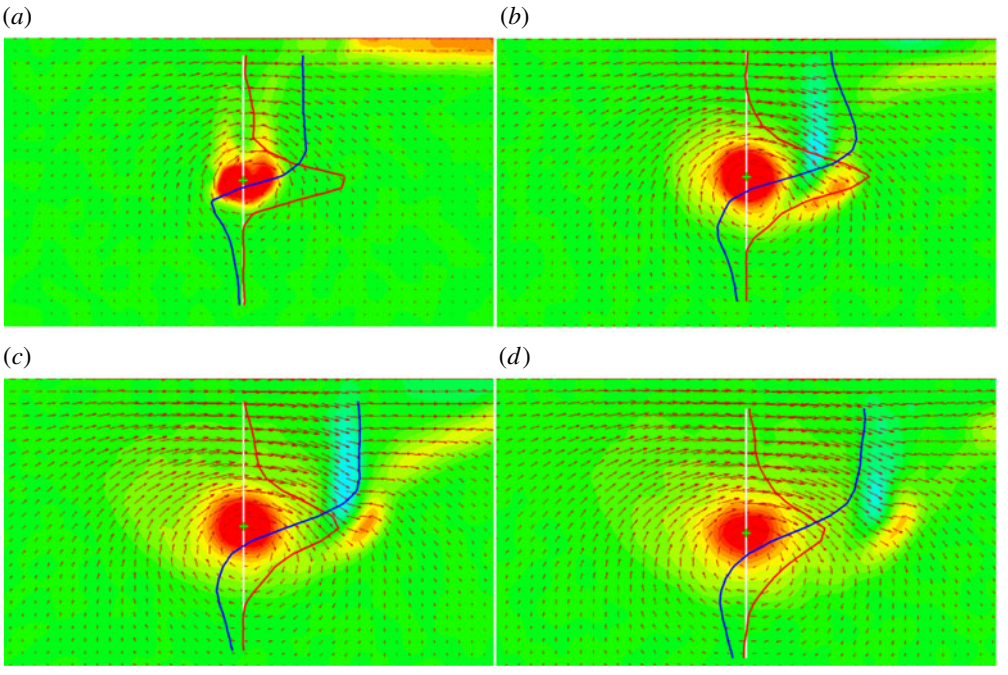


FIGURE 10. Vorticity distribution and x component of the velocity at different times i for disc velocities $U = 5.28$ cm s^{-1} at: (*a*) $t = 0.129$ s, $T_n = 0.226$; (*b*) $t = 0.757$ s, $T_n = 1.333$; (*c*) $t = 1.514$ s, $T_n = 2.665$; (*d*) $t = 2.271$ s, $T_n = 3.998$. The white line passes through the core of the vortex ring (labelled with the green cross mark) and is vertical to the symmetrical axis. The blue and red lines represent the x component of the velocity and the vorticity at the white lines, respectively.

the dimensionless energy of the disc vortex ring first decreases as T_n increases and it ranges from 0.28 to 0.35 at the dimensionless time $T_n = 4$. This value is the same, within experimental error, as the value 0.33 of the jet vortex ring (Gharib *et al.* 1998).

Figure 10 shows the vorticity distribution within the core, where the disc vortex ring evolves from a thin-core vortex ring into an axis-touching vortex ring. Similar to the jet vortex ring, the disc vortex ring possesses a Gaussian vorticity distribution in its core region.

Figures 11 and 12 show the time variations of the position and velocity of the vortex core relative to the disc for different disc velocities. It can be seen that the vortex ring sheds away from the disc gradually and slowly expands outwards along the radial direction. At the first stage of the vortex ring formation, the speed of the vortex core relative to the disc first decreases rapidly and then increases gradually, ultimately reaching the disc speed. It is found that the disc vortex formation process is insensitive to the Reynolds number in our experiments.

As is shown in figure 12 and table 2, at $T_n = 0.2$–0.5 the ratio of the vortex translational velocity to the disc velocity reaches a minimum value of about 0.4–0.5. Moreover, at $T_n = 0.2$, the circulation of the vortex is about 1.3–1.7. Both values correspond well to Taylor's inviscid estimation (Taylor 1953), which gives the dimensionless circulation as 1.27 and the relative speed of the vortex core as 0.436. However, the minimum ratio of the vortex ring radius R_{VR} to the disc radius R_{disc}

https://doi.org/10.1017/jfm.2012.436 Published online by Cambridge University Press

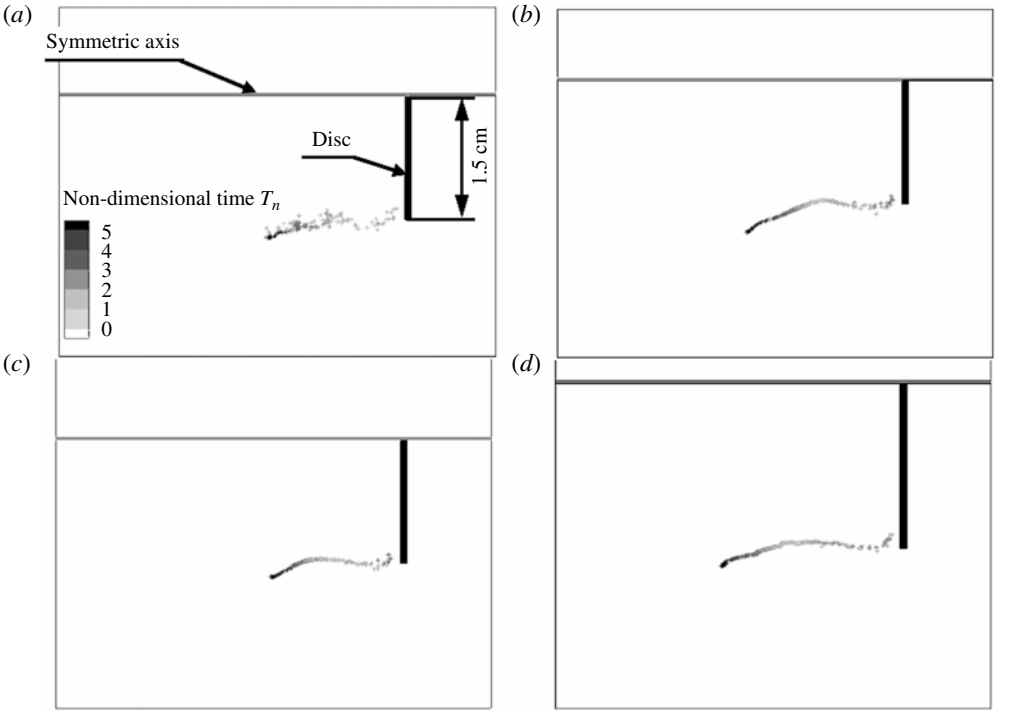


FIGURE 11. Variation of the position of the vortex core relative to the disc.

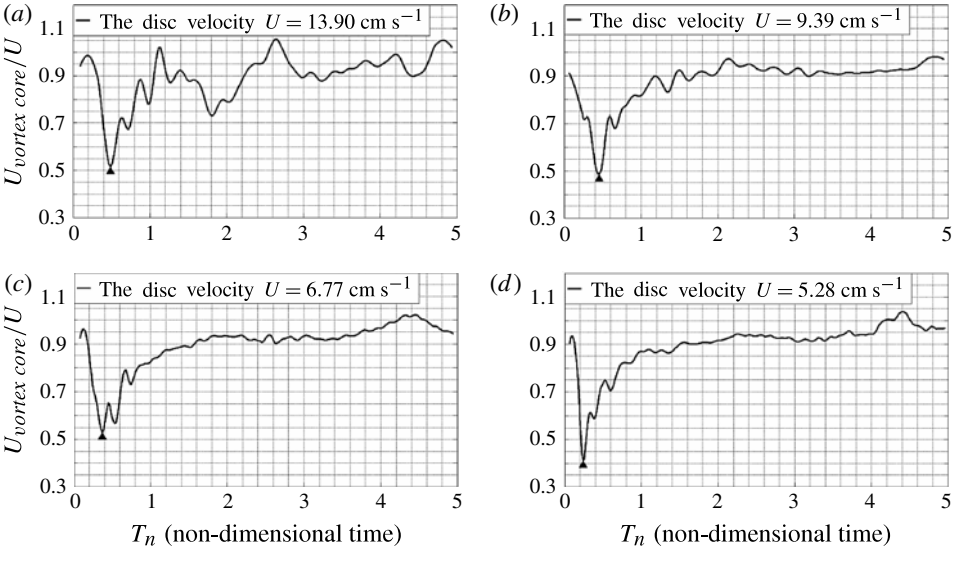


FIGURE 12. Variation of the velocity of the vortex core: (*a*) $U = 13.9$ cm s^{-1}; (*b*) $U = 9.39$ cm s^{-1}; (*c*) $U = 6.77$ cm s^{-1}; (*d*) $U = 5.28$ cm s^{-1}.

https://doi.org/10.1017/jfm.2012.436 Published online by Cambridge University Press

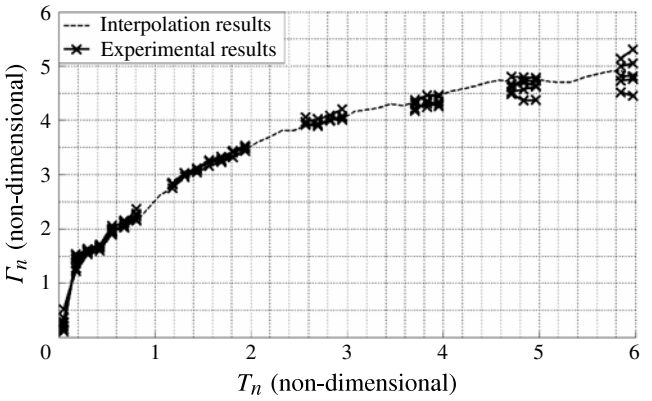


FIGURE 13. Time evolution of the circulation of the disc vortex ring. Each set of crosses corresponds to a single experiment.

U (cm s^{-1})	U_{min}^{VC}/U	T_n^1	R_{min}^{VR}/R_{disc}	T_n^2	$\Gamma_n^{0.2}$
13.9	0.515	0.487	0.918	0.0232	1.6976
9.39	0.487	0.454	0.9345	0.0313	1.5753
6.77	0.530	0.371	0.9291	0.0322	1.2777
5.28	0.413	0.239	0.9181	0.0377	1.3150

TABLE 2. The ratio of the minimum vortex core speed to the disc speed, the ratio of the minimum vortex core radius to the disc radius, and the dimensionless circulation at dimensionless time $T_n = 0.2$. Here U represents the disc velocity, U_{min}^{VC} represents the minimum velocity of the vortex core, T_n^1 represents the dimensionless time corresponding to U_{min}^{VC}, R_{min}^{VR} represents the minimum radius of the vortex ring, T_n^2 represents the dimensionless time corresponding to R_{min}^{VR} and $\Gamma_n^{0.2}$ represents the dimensionless circulation at dimensionless time $T_n = 0.2$.

is ∼0.9, as is shown in table 2, which is larger than that of Taylor's inviscid estimation $R_{VR}/R_{disc} = 0.816$.

6. Flow field of the vortex ring when the dimensionless time $T_n > 5$

The results represented above are for the dimensionless time $T_n \leqslant 5$. It is found that in our experiments the flow field of the disc vortex ring evolves into an obvious non-axisymmetric state when $T_n > 5$. In such a case the disc vortex ring cannot be obtained quantitatively by the two-dimensional PIV and only qualitative results are shown below.

Figure 13 illustrates the experimental data of the dimensionless circulations under different manipulation processes, where the interpolation result is also plotted. When $T_n < 4$, the circulations of the experiments possess high consistency and the interpolation curve fits well. However, when the dimensionless time $T_n \geqslant 4$, the circulations exhibit an obvious tendency of dispersion and deviate from the interpolation curve, implying that our experiments are not repeatable in this situation. In order to illuminate the origin of this derivation, we conduct the flow visualization

https://doi.org/10.1017/jfm.2012.436 Published online by Cambridge University Press

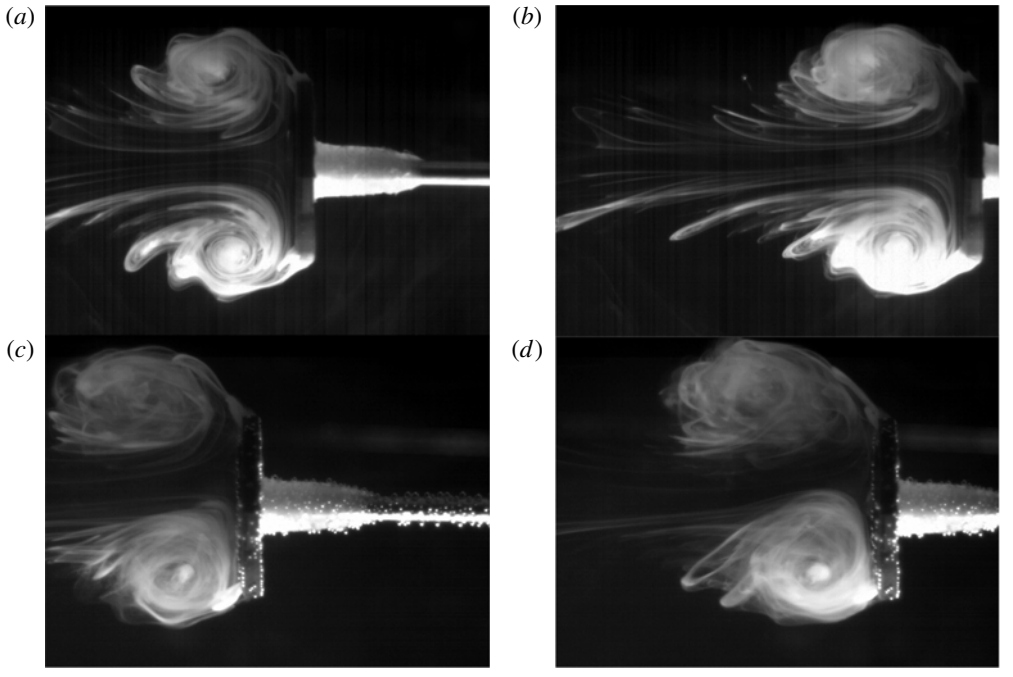


FIGURE 14. Images of the disc vortex rings at the disc velocity $U = 5.28$ cm s^{-1}: (*a*) $T_n = 3.84$; (*b*) $T_n = 4.71$; (*c*) $T_n = 5.31$; (*d*) $T_n = 6.01$.

experiments using milk in a symmetrical plane (figure 14). It can be seen from the figure that the vortex ring maintains symmetry until $T_n \geqslant 4$ and exhibits an obvious asymmetric three-dimensional characteristic when $T_n \geqslant 5$. The result of the DPIV in figure 15 further demonstrates this phenomenon. Note that in the figure there are several calculation errors near the symmetric axis, which do not occur when $T_n \leqslant 5$. The appearance of these computation errors indicates that there exists a large off-plane velocity in the flow field of the vortex ring.

In the case of the jet vortex ring, after the formation of the jet vortex ring the jet behaves unstably. In the case of the disc vortex ring, when the circulation attains saturation the axisymmetric vortex ring also becomes unstable and ultimately evolves into a three-dimensional structure. However, it should be noted that they are due to different mechanisms.

7. Time evolution of the hydrodynamic force on the disc

The hydrodynamic force imposed on a body immersed in a fluid can be calculated using the DPIV data measured in experiments. Basically there are three methods: the vorticity-free analysis method (VFAM) (Peng *et al.* 2007), the vorticity-moment method (VMM) (Saffman 1992; Wu 2005) and the direct momentum conservation method (DMCM). In this paper, the time evolution of the impulse on the disc is calculated using the DMCM and VMM. The VFAM is not adopted because of the difficulty in calculating the added-mass coefficient.

https://doi.org/10.1017/jfm.2012.436 Published online by Cambridge University Press

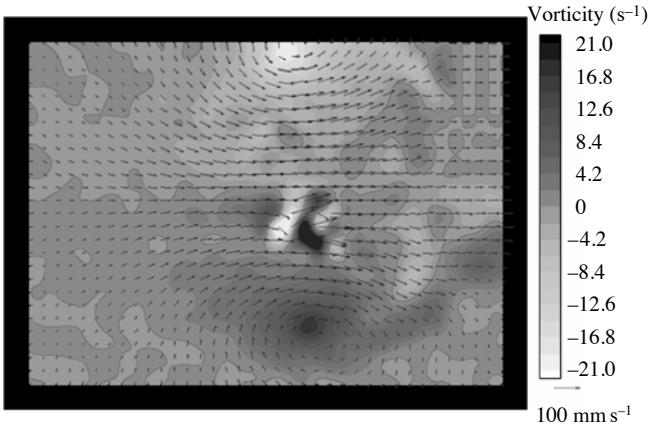


FIGURE 15. Graphic velocity vector and vorticity for $U = 5.28$ cm s^{-1} at the dimensionless time $T_n = 6.02$.

7.1. *Vorticity-moment method (VMM)*

According to the vorticity-moment theorem (Saffman 1992; Wu 2005), the hydrodynamic force $\boldsymbol{F}$ exerted by the fluid on the solid immersed in and moving relative to the fluid is written as

$$\boldsymbol{F} = -\frac{\rho}{2}\frac{\mathrm{d}}{\mathrm{d}t}\iiint_{V_\infty} \boldsymbol{x} \times \boldsymbol{\omega}\,\mathrm{d}V + \rho\frac{\mathrm{d}}{\mathrm{d}t}\iiint_{V_s} \boldsymbol{U}\,\mathrm{d}V, \tag{7.1}$$

where V_s is the region occupied by the solid, V_∞ is the infinite unlimited space occupied jointly by the fluid and the solid, $\boldsymbol{U}$ is the velocity field, $\boldsymbol{\omega}$ is the vorticity field, ρ is the density and $\boldsymbol{x}$ is the position vector. The axisymmetric form of (7.1) in cylindrical coordinates is

$$D = -\frac{\rho}{2}\frac{\mathrm{d}}{\mathrm{d}t}\iiint_{V_\infty} r\omega_\theta\,\mathrm{d}V = -\frac{\rho}{2}\frac{\mathrm{d}}{\mathrm{d}t}\iint_{s} r\omega_\theta\,2\pi r\,\mathrm{d}s, \tag{7.2}$$

where ω_θ is the θ component of the vorticity and r is the radial coordinate. VMM is valid in the unbounded viscous fluid. In the calculation, the computational domain needs to be large enough to enclose all of the vorticity flux.

7.2. *Direct momentum conservation method (DMCM)*

Take an arbitrary control surface enclosing the disc. According to the momentum conservation theorem, the total force exerted by the disc on the fluid contains three parts (figure 16): the variation rate of the momentum of the fluid enclosed by the control surface ($\mathrm{d}I_1/\mathrm{d}t$), the integral of the pressure on the control surface ($\mathrm{d}I_2/\mathrm{d}t$), and the momentum flux of the fluid through the control surface ($\mathrm{d}I_3/\mathrm{d}t$). The three parts of the momentum in the x direction are

$$I_{1x} = \iiint u_x^t\,\mathrm{d}V - \iiint u_x^{t_0}\,\mathrm{d}V, \tag{7.3}$$

$$I_{2x} = \int_{t_0}^{t} \oiint \Delta p n_x\,\mathrm{d}S\,\mathrm{d}t, \tag{7.4}$$

$$I_{3x} = \int_{t_0}^{t} \oiint (\boldsymbol{u}\cdot\boldsymbol{n})u_x\,\mathrm{d}S\,\mathrm{d}t. \tag{7.5}$$

https://doi.org/10.1017/jfm.2012.436 Published online by Cambridge University Press

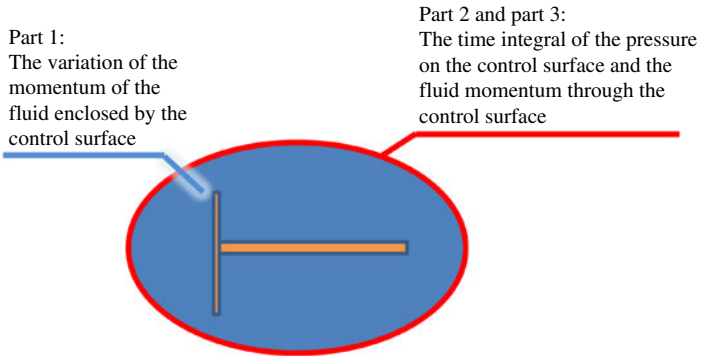


FIGURE 16. (Colour online) Schematic of the three parts of the impulse exerted by the disc on the fluid.

Parts 1 and 3 can be obtained straightforwardly from the DPIV data. However, part 2 is difficult to calculate because of the unknown pressure on the control surface. Fortunately, the flow may be regarded as potential outside the control surface. (The Reynolds number of the flow ranges from 1600 to 4200 based on the disc speed U and diameter D in our experiments. Based on the Reynolds number and the disc vortex ring formation time, the distance of the viscous diffusion $\delta \ll D$.) According to the unsteady Bernoulli equation,

$$\frac{\partial \varphi}{\partial t} + \frac{\boldsymbol{u}^2}{2} + \int \frac{\mathrm{d}p}{\rho} + \Psi = C, \tag{7.6}$$

where φ ($\varphi = \varphi_0 + \int \boldsymbol{u} \cdot \mathrm{d}\boldsymbol{l}$) is the velocity potential, $\boldsymbol{u}$ is the velocity, p is the pressure, ρ is the fluid density, Ψ is the body force potential and C is a constant. Considering that the body force is neglected and the fluid density is constant, (7.6) yields

$$\Delta p = -\frac{\partial \varphi}{\partial t} - \frac{\boldsymbol{u}^2}{2} + C, \tag{7.7}$$

where Δp ($\Delta p = p - p_\infty$) is the pressure difference and p_∞ is the pressure at infinity. Substituting (7.7) into (7.4), part 2 is rewritten as

$$\begin{aligned} I_{2x} &= \int_{t_0}^{t} \oiint \frac{\partial \varphi}{\partial t} n_x \,\mathrm{d}S \,\mathrm{d}t - \int_{t_0}^{t} \oiint \frac{1}{2} (\boldsymbol{u})^2 n_x \,\mathrm{d}S \,\mathrm{d}t \\ &= \oiint -\varphi^t n_x \,\mathrm{d}S + \oiint \varphi^{t_0} n_x \,\mathrm{d}S - \int_{t_0}^{t} \oiint \frac{1}{2} (\boldsymbol{u})^2 n_x \,\mathrm{d}S \,\mathrm{d}t. \end{aligned} \tag{7.8}$$

Combining the third term on the right-hand side of (7.8) with (7.5), the three new parts of the total impulse, I'_{1x}, I'_{2x} and I'_{3x}, are obtained, i.e.

$$I'_{1x} = I_{1x} = \iiint u_x^t \,\mathrm{d}V - \iiint u_x^{t_0} \,\mathrm{d}V, \tag{7.9}$$

$$I'_{2x} = \oiint -\varphi^t n_x \,\mathrm{d}S - \oiint -\varphi^{t_0} n_x \,\mathrm{d}S, \tag{7.10}$$

$$I'_{3x} = \int_{t_0}^{t} \oiint \left[(\boldsymbol{u} \cdot \boldsymbol{n}) u_x - \frac{1}{2} \boldsymbol{u}^2 n_x \right] \mathrm{d}S \,\mathrm{d}t. \tag{7.11}$$

https://doi.org/10.1017/jfm.2012.436 Published online by Cambridge University Press

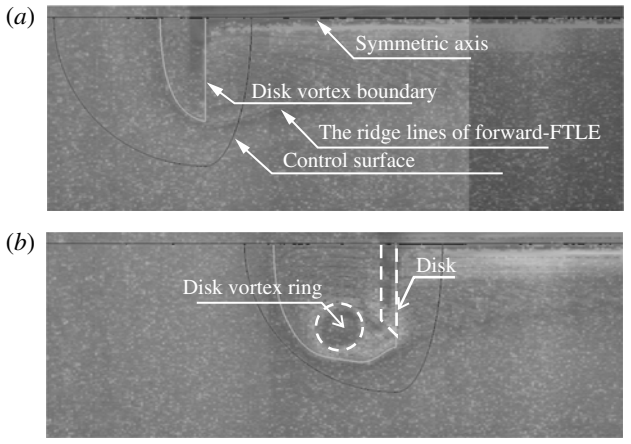


FIGURE 17. The outline of the vorticity-free control surface for $U = 6.77\ \mathrm{cm\ s^{-1}}$ at: (*a*) $t = 0$ s; (*b*) $t = 0.643$ s. The semitransparent map is obtained by superimposing the particle image, the forward-time FTLE map, the velocity vector graphics and vorticity map. The black lines represent the symmetric axis. The yellow lines represent the disc vortex boundary defined in § 4. The red lines represent the vorticity-free control surface chosen for the time period from $t = 0$ to $t = 0.643$ s.

Because I'_{1x} and I'_{2x} are functions of state variables, there are no accumulative errors in the calculation process for these two parts. However, I'_{3x} is a process variable. Fortunately, it is small compared to I'_{1x} and I'_{2x}, only accounting for at most 6 % of the impulse exerted by the disc on the fluid.

In our experiments, the duration $t < 3$ s and the kinematic viscosity $\nu = 10^{-6}\ \mathrm{m^2\ s^{-1}}$ lead to the viscosity characteristic length $\delta = \sqrt{\gamma t} \leqslant 1.7$ mm, which is much smaller than the vortex characteristic length $D = 30$ mm. Therefore, the potential flow hypothesis is valid for the disc vortex flow outside the control surface. Since the LCS is a material line, the vorticity cannot cross it. For the disc vortex flow, a vorticity-free control surface enclosing the LCS can always be found (as is shown in figure 17) and the potential flow hypothesis is valid for flows outside the vorticity-free control surface.

The magnitude of the fluid velocity surrounding the control surface should be as large as possible in order to diminish the relative error of the pressure calculation. Therefore, to satisfy the potential flow hypothesis and the velocity magnitude condition simultaneously, an appropriate control surface is chosen for different time periods as shown in figure 17. Additionally, it is shown that the vorticity-free control surface moved with the disc, so the disc velocity U should be subtracted from the fluid velocity in the calculation. Replacing $\boldsymbol{u}$ with $\boldsymbol{u}' = \boldsymbol{u} - \boldsymbol{U}$ in (7.9)–(7.11), all the additional terms induced by $\boldsymbol{U}$ are eliminated in the incompressible condition.

7.3. *Time evolution of the impulse on the disc*

Figure 18 shows the temporal impulse exerted by the disc on the fluid calculated by the DMCM and VMM for different disc speeds. Obviously, in all the situations, the results of the two methods agree well with each other. The trends of the temporal impulse are similar to those of the temporal circulation, with the impulse increasing with disc velocity. The corresponding dimensionless results are shown in

https://doi.org/10.1017/jfm.2012.436 Published online by Cambridge University Press

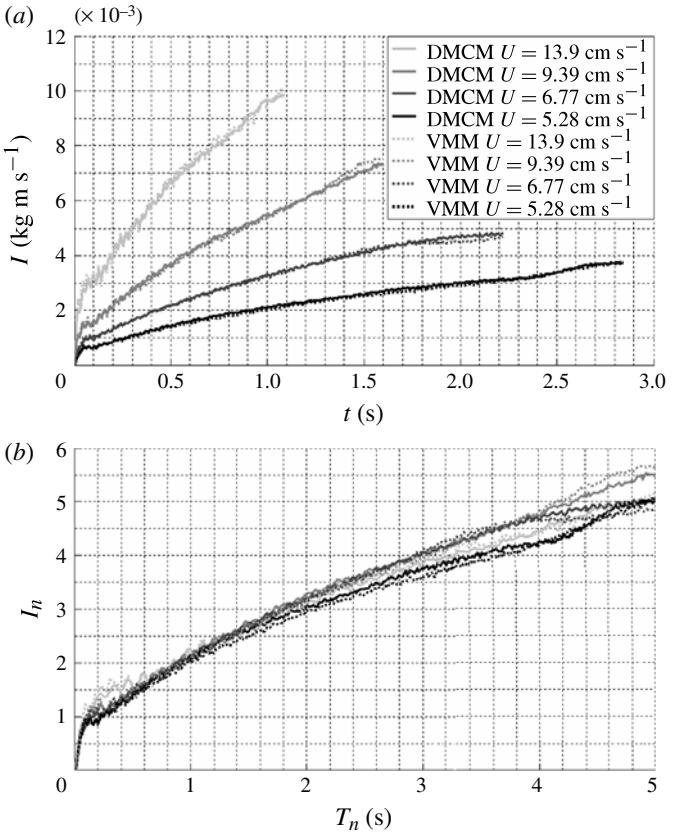


FIGURE 18. Temporal impulse exerted by the disc on the fluid calculated by the direct momentum conservation method (DMCM) and vorticity momentum method (VMM): (*a*) the dimensional results; (*b*) the dimensionless results.

figure 18(*b*), where the specific impulse $I_c = \rho V_c U$ is taken as the characteristic scale. The dimensionless impulses at different disc velocities coincide well with each other.

Figure 19 shows that the ratio of I'_{1x} (the momentum of the fluid enclosed by the control surface) to I_x (the impulse exerted by the disc on the fluid) increases up to $T_n = 3$ and holds a value between 0.64 and 0.68 for $T_n > 3$. As is well known, the ratio of the impulse exerted by the disc on the fluid to the momentum of the disc vortex ring, after subtracted by 1, equals the added-mass coefficient. Figure 20 shows that this ratio ranges from 1.4 to 1.6 and the corresponding added-mass coefficient ranges from 0.4 to 0.6.

8. Discussion and conclusion

In this paper we describe an experimental study on the kinematic and dynamic characteristics of a vortex ring caused by the impulsive starting of a circular disc. The FTLE field and LCSs are calculated based on the data obtained from the experiments. During the formation process of the disc vortex ring, the fluid is found to be possibly divided into three parts by the disc and the r-LCS. The fluid outside the r-LCS cannot be entrained into the vortex ring. The fluid inside the r-LCS and leeward of the disc

https://doi.org/10.1017/jfm.2012.436 Published online by Cambridge University Press

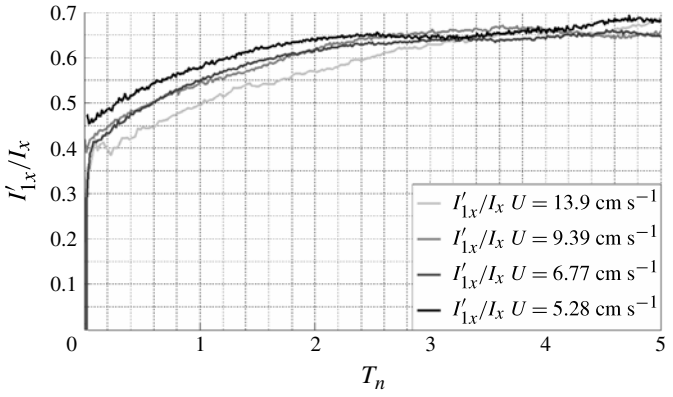


FIGURE 19. The ratio of I'_{1x} (the momentum of the fluid enclosed by the control surface) to I_x (the impulse exerted by the disc on the fluid).

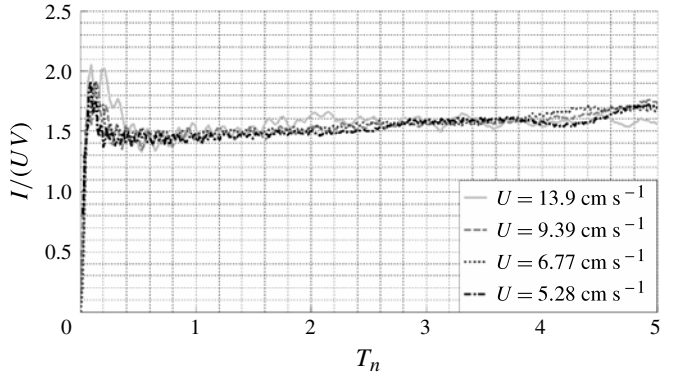


FIGURE 20. The ratio of I_x (the impulse exerted by the disc on the fluid) to UV (the impulse of the disc vortex ring), where the velocity of the disc vortex ring equals the disc velocity U.

moves together with the disc vortex ring during the whole process and it is entrained gradually into the vortex ring. Owing to the existence of the disc, the fluid in the front of the disc and inside the r-LCS flows into the vortex ring through the unique flux window between the disc and the r-LCS.

The boundary of the vortex ring consists of the r-LCS leeward, the disc and the flux window. The volume, circulation and dimensionless energy of the disc vortex are calculated. In addition, the temporal position of the vortex core in the formation process of the ring is obtained. The limiting value of dimensionless time is found to be approximately 5. Beyond this value the disc vortex ring exhibits an obvious non-axisymmetric characteristic. According to the flow patterns of the disc vortex ring and the repeatability test through calculating the circulation of the disc vortex rings, the axisymmetric disc vortex ring begins to become non-axisymmetric at $T_n = 4$. However, this process is gradual. Keeping the macroscopic quantities of the disc vortex rings at the dimensionless time $4 \leqslant T_n \leqslant 5$ is acceptable as a rough estimate.

The formation process of the disc vortex ring can be roughly divided into three phases. The first is a rapid growth phase for the dimensionless time $0 < T_n < 0.2$,

https://doi.org/10.1017/jfm.2012.436 Published online by Cambridge University Press

with the growth rate of the circulation much larger than 1. At the dimensionless time $T_n \approx 0.2$, the vortex translational velocity reaches a minimum of 0.4–0.5 of the disc velocity, and the dimensionless circulation of the vortex ring is about 1.3–1.7. Both agree well with Taylor's inviscid estimation. It is verified that Taylor's inviscid estimation does work at the beginning of the disc vortex formation process. This means that the formation mechanism of the disc vortex ring at the beginning obeys Taylor's inviscid theory.

The second is a stable growth phase for about $0.2 < T_n < 4$, in which the growth rate of the dimensionless circulation $\mathrm{d}\Gamma_n/\mathrm{d}T_n$ is close to 2 at the beginning and then decreases gradually, as shown in figure 8(*c*). In this phase, the disc vortex ring changes from a thin core vortex ring into an axis-touching vortex ring, its dimensionless energy decreasing gradually. At the end of this phase or later, the disc vortex ring possesses a Gaussian vorticity distribution in its core the same as the jet vortex ring; the circulation, volume and dimensionless energy of the disc vortex ring reach saturation. It is concluded that the disc vortex ring reaches 'saturation state' when $T_n \approx 4$. Owing to the unavailability of the three-dimensional velocity field data or the three-dimensional flow visualization of the disc vortex ring, this saturation moment cannot be determined accurately.

The last is a non-axisymmetric phase at the dimensionless time $T_n \gtrsim 4$. After the saturation of the circulation, the disc vortex ring loses symmetry. The mechanism of this phase is probably the instability of the axisymmetric vortex ring. As mentioned above, when the dimensionless time $4 \leqslant T_n \leqslant 5$, the circulation, volume and dimensionless energy of the disc vortex ring change little. Therefore, for such a period, the saturated macroscopic quantities of the disc vortex ring can be estimated. The saturated dimensionless volume V_n of the disc vortex ring is $\sim$3.1–3.4, and the entrained fluid fraction $\eta(t)$ is 12 %, which is much less than the jet vortex ring; the saturated dimensionless circulation is 4.5–4.9, slightly larger than that of the jet vortex ring; the dimensionless energy of the disc vortex ring reaches the minimum of 0.28–0.35, close to 0.33 of the jet vortex ring.

Comparing the two kinds of vortex rings, there are several differences and similarities between the jet and disc vortex rings. The differences: (i) the entrained fluid fraction of the disc vortex ring is that of the jet vortex ring; and (ii) the saturation characteristic of the jet vortex ring is 'pinch-off', but that of the disc vortex ring is non-axisymmetry. The similarities: (i) for the jet and disc vortex rings, the dimensionless times generating the vorticity fluxes that enter into the vortex rings are both about 4; (ii) the jet and disc vortex rings both have a thin Gaussian-like core at the beginning of the formation process, and an axis-touching core at the end of the formation process; and (iii) the dimensionless energy of the saturated disc is close to that of the jet vortex ring.

Acknowledgements

This work was supported by the NSFC (grants 10832010 and 11002138), the Innovation Project of CAS (grant KJCX2-YW-L05), and the China Postdoctoral Science Foundation (grant 20090460733). The authors would like to thank Dr P. F. Linden and the referees for their suggestions and help.

https://doi.org/10.1017/jfm.2012.436 Published online by Cambridge University Press

Appendix. Notation

Time:	t
Fluid density:	ρ
Disc diameter:	D
Disc velocity:	U
Vortex ring circulation:	Γ
Vortex ring volume:	V
Impulse exerted by the disc on the fluid:	I_x
Characteristic circulation:	$\Gamma_c = \frac{1}{2}UD$
Characteristic volume:	$V_c = \frac{1}{6}\pi D^3$
Characteristic impulse:	$I_c = \rho V_c U$
Dimensionless time:	$T_n = tU/D$
Dimensionless circulation:	$\Gamma_n = \Gamma/\Gamma_c = \Gamma/(\frac{1}{2}UD)$
Dimensionless volume:	$V_n = V/V_c = V/(\frac{1}{6}\pi D^3)$
Dimensionless impulse:	$I_{nx} = I_x/(\rho V_c U) = I_x/(\rho \frac{1}{6}\pi D^3 U)$

REFERENCES

DABIRI, J. O. 2009 Optimal vortex formation as a unifying principle in biological propulsion. *Annu. Rev. Fluid Mech.* **41**, 311–331.

DABIRI, J. O. & GHARIB, M. 2004 Fluid entrainment by isolated vortex rings. *J. Fluid Mech.* **511**, 311–331.

GHARIB, M., RAMBOD, E. & SHARIFF, K. 1998 A universal time scale for vortex ring formation. *J. Fluid Mech.* **360**, 121–140.

GREEN, M. A., ROWLEY, C. W. & HALLER, G. 2007 Detection of Lagrangian coherent structures in three-dimensional turbulence. *J. Fluid Mech.* **572**, 111–120.

HALLER, G. 2001 Distinguished material surfaces and coherent structures in three-dimensional flows. *Physica* D **149**, 248–277.

HALLER, G. 2002 Lagrangian coherent structures from approximate velocity data. *Phys. Fluids* **14**, 1851–1861.

HIGUCHI, H. & BALLIGAND, H. 1996 Numerical and experimental investigations of the flow over a disk undergoing unsteady motion. *J. Fluids Struct.* **10**, 705–719.

LINDEN, P. F. & TURNER, J. S. 2001 The formation of 'optimal' vortex rings, and the efficiency of propulsion devices. *J. Fluid Mech.* **427**, 61–72.

PENG, J., DABIRI, J. O., MADDEN, P. G. & LAUDER, G. V. 2007 Non-invasive measurement of instantaneous forces during aquatic locomotion: a case study of the Bluegill Sunfish pectoral fin. *J. Expl Biol.* **210**, 685–698.

ROSENFELD, M., RAMBOD, E. & GHARIB, M. 1998 Circulation and formation number of laminar vortex ring. *J. Fluid Mech.* **376**, 297–318.

SAFFMAN, P. G. 1992 *Vortex Dynamics*. Cambridge University Press.

SALLET, D. W. 1975 Impulsive motion of a circular disk which causes a vortex ring. *Phys. Fluids* **18**, 109–111.

SHADDEN, S. C., DABIRI, J. & MARSDEN, J. 2006 Lagrangian analysis of fluid transport in empirical vortex ring flows. *Phys. Fluids* **18**, 047105.

SHADDEN, S. C., KATIJA, K., ROSENFELD, M., MARSDEN, J. E. & DABIRI, J. O. 2007 Transport and stirring induced by vortex formation. *J. Fluid Mech.* **593**, 315–331.

SHADDEN, S. C., LEKIEN, F. & MARSDEN, J. 2005 Definition and properties of Lagrangian coherent structures from finite-time Lyapunov exponents in two-dimensinal aperiodic flows. *Physica* D **212**, 271–304.

SHARIFF, K. & LEONARD, A. 1992 Vortex rings. *Annu. Rev. Fluid Mech.* **24**, 235–279.

SHENOY, A. R. & KLEINSTREUER, C. 2008 Flow over a thin circular disk at low to moderate Reynolds numbers. *J. Fluid Mech.* **605**, 253–262.

TAYLOR, G. I. 1953 Formation of a vortex ring by giving an impulse to a circular disc and then dissolving it away. *J. Appl. Phys.* **24**, 104–105.

https://doi.org/10.1017/jfm.2012.436 Published online by Cambridge University Press

WILLERT, C. E. & GHARIB, M. 1991 Digital particle image velocimetry. *Exp. Fluids* **10**, 181–193.

WU, J. C. 2005 *Elements of Vorticity Aerodynamics*. Tsinghua University Press.

YANG, A., JIA, L. & YIN, X. 2010 Experimental study of a starting vortex ring produced by a thin circular disk. *J. Biomed. Engng* **7**, S103–S108.

https://doi.org/10.1017/jfm.2012.436 Published online by Cambridge University Press